Rational design of mixed-matrix metal-organic framework membranes for molecular separations

Rational design of mixed-matrix metal-organic framework membranes for molecular separations

Shuvo Jit Datta[1,2], Alvaro Mayoral[3,4,5], Narasimha Murthy Srivatsa Bettahalli[1], Prashant M. Bhatt[1,2], Madhavan Karunakaran[1]ϕ, Ionela Daniela Carja[2], Dong Fan[6], Paulo Graziane M. Mileo[6], Rocio Semino[6], Guillaume Maurin[6], Osamu Terasaki[3,4], Mohamed Eddaoudi[1,2]*

Conventional separation technologies to separate valuable commodities are energy-intensive, consuming 15% of the worldwide energy. Mixed-matrix membranes, combining processable polymers and selective adsorbents, offer potential to deploy adsorbent distinct separation properties into processable matrix. We report a rational design and construction of highly-efficient mixed-matrix metal-organic framework membrane based on three interlocked criteria: i) fluorinated metal-organic framework, AlFFIVE-1-Ni as molecular sieve adsorbent that selectively enhanced H_2S and CO_2 diffusion while excluding CH_4. ii) Tailoring - crystal morphology into nanosheets with maximally exposed (001)-facets. iii) In-plane alignment of (001)-nanosheets in polymer matrix and attainment of [001]-oriented membrane. The membrane demonstrated exceptionally high H_2S and CO_2 separation from natural gas under practical working conditions. This approach offers great potential to translate other key adsorbents into processable matrix.

[1]Division of Physical Science and Engineering, Advanced Membrane and Porous Materials Center, King Abdullah University of Science and Technology (KAUST), Thuwal 23955-6900, Kingdom of Saudi Arabia. [2]Division of Physical Science and Engineering, Advanced Membrane and Porous Materials Center, Functional Materials Design, Discovery and Development (FMD[3]), KAUST, Thuwal 23955-6900, Kingdom of Saudi Arabia. [3]Centre for High-resolution Electron Microscopy, School of Physical Science and Technology, ShanghaiTech University, Shanghai 201210, China. [4]Shanghai Key Laboratory of High-resolution Electron Microscopy, ShanghaiTech University; Shanghai, 201210, China. [5]Instituto de Nanociencia y Materiales de Aragon, CSIC-Universidad de Zaragoza; Laboratorio de Microscopias Avanzadas, Zaragoza, Spain. [6]ICGM, Univ. Montpellier, CNRS, ENSCM, Montpellier, France.

*e-mail: mohamed.eddaoudi@kaust.edu.sa

ϕPresent address: Centre For Carbon Fiber and Prepregs, CSIR-National Aerospace Laboratories, Bengaluru 560017, India.

Chemical separations are highly energy-intensive and account for around half of the global industrial energy consumption (*1, 2*). Membrane-based separation can provide an energy-efficient alternative to traditional separation processes like cryogenic distillation and adsorptive separation. Polymer membranes intrinsically undergo a trade-off between the permeability (productivity) and selectivity (efficiency), known as Robeson's upper bound (*3, 4*). Mixed-matrix membranes (MMMs), combining the distinct properties of selective adsorbents (molecular separation and facilitated gas transport) and polymers (processability and mechanical stability), may enable energy-efficient and environmentally sustainable technologies (*5-7*). Nevertheless, successful translation of adsorbent distinct properties into MMMs remains a persistant challenge, due to recurring agglomeration and sedimentation of adsorbent fillers in the polymer matrix and incompatibility between adsorbent-polymer interfaces. As a result of these challenges, the attainment of highly selective membranes is hampered as well as the mechanical properties of the membranes are lessened (*8*).

Various MMMs have been reported, using isotropic or near-anisotropic fillers (*6, 7, 9*), and these membranes exhibited moderate improvement in selectivity and/or permeability (*7, 10, 11*). The impact of filler particle size (*12*), morphology (*6, 13*), functionality (*14*), and surface modification (*15*) in MMMs on gas separation are well documented. An anisotropic morphology, like high-aspect-ratio nanosheets, was recognized to offer several advantages over isotropic fillers. The relatively large external surface area proffers an enhancement of the nanosheets-polymer interface compatibility, permitting high filler loading, while the combination of very short gas diffusion pathways with preserved molecular discrimination may result in a considerable increase of both permeability and selectivity (*16*).

Only a limited number of metal-organic framework (MOF) nanosheets have been explored in MMMs for gas separation (*17-22*). Cu-BDC nanosheets (from 2D layer-structured MOF) was first embedded in Matrimid polymer in a form of MMM for CO_2/CH_4 separation *(17)*. The membrane showed moderate selectivity improvement at the expense of a lower CO_2 permeability, plausibly due to none-selective nor promoted transport of CO_2 versus CH_4 in the relatively larger pore system (~6.5 Å). NH_2-MIL-53(Al), a 3D periodic framework with a relatively strong CO_2 interactions, was prepared as nanosheets using CTAB surfactant (*18*)). Unfortunately, the resultant MMM showed a relatively moderate CO_2/CH_4 separation, plausibly due to residual CTAB on the surface of nanosheets affecting the gas separation properties of the pristine material, pinpointing to the importance of surfactant-free nanosheets preparation. Methods to use contracted pore and/or better performing MOF structures as defect-free nanosheets is of prime importance, as numerous contracted pore MOF structures offer desirable adsorption and molecular diffusion properties

(*23*) but they are not ideal for conventional exfoliation methods (*24*). In addition to the attainment of high-aspect-ratio nanosheets of desired MOFs, it is essential to develop suitable strategies that can afford requisite alignment of nanosheets within the polymer matrix.

We report a concept for the construction of a mixed-matrix metal-organic framework (MMMOF) membrane based on three interlocked criteria: i) a MOF filler possesses optimal pore size and shape, functionality, host-guest interaction that selectively enhanced H_2S and CO_2 diffusion while excluding CH_4. ii) Tailoring MOF crystal morphology along 001 crystallographic direction into high-aspect-ratio (001)-nanosheets that proffers maximum exposure of one-dimensional (1D) channel and promotes nanosheets-polymer interaction resultant high nanosheets loading. iii) In-plane (face-to-face) alignment of (001)-nanosheets in polymer matrix with proximal distance to translate the molecular separation properties of single nanosheets into a uniformly [001]-oriented macroscopic MMMOF membrane.

Hydrolytically stable fluorinated AlFFIVE-1-Ni (KAUST-8), when used as an adsorbent, showed excellent separation properties for H_2S/CH_4 and CO_2/CH_4 (*25, 26*). This MOF possesses appropriate H_2S and CO_2 adsorption and separation properties, high chemical stability towards H_2S that instigate AlFFIVE-1-Ni as a potential molecular sieve filler in MMMOF membrane for natural gas upgrading. However, effective deployment of AlFFIVE-1-Ni (a 3-periodic MOF with 1D channels) as a filler into membranes, requires its morphology to be tailored into nanosheets with defined crystallographic direction, for maximum surface exposure of 1D channels (*25, 26*).

The structure of AlFFIVE-1-Ni along the [110] or [1-10] direction is shown in Fig. 1A. The 2-periodic square-grid layer constructed by linking Ni(II) with pyrazine ligand are pillared by $[AlF_5(H_2O)]^{2-}$ anions in the third dimension to construct a 3-periodic framework/structure with the primitive cubic (pcu) underlying topology and pore walls comprised of $[AlF_5(H_2O)]^{2-}$ anions, prohibiting access to the pore system in [110] and [1-10] direction (Fig. 1A). Schematic illustrations of a typical truncated-bipyramidal morphology of the crystal and its channel orientation are shown in Fig. 1B. The structure consists of 1D ultra-small channels (represented in green) that run along the [001] direction (Fig. 1, B and C). These channels are accessible to only relatively small gas molecules (*e.g.* He, H_2, CO_2, O_2, H_2S, N_2 etc.).

Synthesis and characterization of MOF nanosheets

A scanning electron microscopy (SEM) image of AlFFIVE-1-Ni crystals obtained by conventional hydrothermal synthesis, suggesting the material is not suitable for membrane fabrication (fig. S1). Grinding large particles into nanoparticles may not improve their gas separation performances as the majority of the nanoparticles may expose the non-accessible (110) and (1-10) facets. The 1D channels of

AlFFIVE-1-Ni can only be fully exploited if the morphology is controlled into nanosheets with completely exposed (001) facets. Therefore, the crystallographic growth along *c*-direction must be significantly reduced or completely suppressed relative to the desired growth along *a*- and *b*-directions. We develop a bottom-up synthesis approach yielding high-aspect-ratio nanosheets. Performing the synthesis under a reduced $[AlF_5(H_2O)]^{2-}$ pillaring units concentration along with decreasing synthesis temperature promoted the formation of crystals with large lateral dimensions and prevented the growth in the *c*-direction (Fig. 1A, see supplementary materials and figs. S1 and S2). Further, the addition of ethanol into the reaction mixture was found to be very effective to further reduce crystal thickness while maintaining the nanosheets morphology (fig. S3).

Diverse MOF nanosheets have been prepared either from 2D layer-structured MOFs by exfoliation methods (*27*) or from 3D periodic framework by 2D oxide sacrifice approach (*28*) and/or surfactant-assisted synthesis (*18, 29*). We present a bottom-up synthesis method for the preparation of MOF nanosheet from a 3D periodic fluorinated MOF with contracted pore system (*25*). Importantly, we did not use surfactant, modulator, or template, and synthesis was accomplished at relatively low temperature (55 °C) resultant nanosheets are defect-free (STEM analyses) and undesirable substance-free, the essential requirements for membrane application. The optimized synthesis method differs from the bulk synthesis (*25*) and is scalable (fig. S4).

Adjusting the synthesis conditions afforded the crystal morphology control from aggregated truncated bipyramidal morphology to nanosheets (Fig. 1D and figs. S1 to S3). SEM images reveal that synthesized square-shaped nanosheets exhibit an average lateral dimension of 0.5-4 μm and thickness in the range of 20-50 nm, resulting in an aspect ratio greater than 25 (Fig. 1D). A scanning transmission electron microscopy (STEM) image of nanosheets (Fig. 1E) corroborates the higher aspect ratio. The nanosheets dispersion is supported by the observed Tyndall effect using a green laser (Fig. 1E, inset, and Movie S1). Powder X-ray diffraction (PXRD) pattern of the material (Fig. 1G), shows preferred orientation effect of (001)-nanosheets with the 00*l* (*l*=2n) reflections significantly enhanced, further confirming the successful synthesis of nanosheets with AlFFIVE-1-Ni structure.

In addition, we developed a synthesis method to produce nanoparticles (Fig. 1F). SEM images reveal that nanoparticles are fairly uniform with particle size *ca*. 50-120 nm and PXRD confirmed AlFFIVE-1-Ni structure (Fig. 1G). The CO_2 sorption isotherms affirm that bulk material, nanosheets and nanoparticles exhibit similar CO_2 uptake capacity (fig. S5). Variable temperature CO_2 adsorption isotherms on

nanosheets are shown (Fig. 1H). The versatility and scope of our MOF nanosheets synthetic strategy was further evaluated with the fabrication of the FeFFIVE-1-Ni (KAUST-9) nanosheets (fig. S6) (*25*).

Atomic structure analysis of MOF nanosheets

Annular Bright-Field (ABF) images taken with the C_s-corrected STEM from the nanosheet along the [001] and the [100] directions were shown in Fig 2, A and D, respectively. The images offer an unambiguous visualization of the atomic structure, and the corresponding Fourier Diffractogram (FD), and selected area electron diffraction (SAED) pattern were inserted at the top right in the images with indices based on the space group *I*4/*mcm* with *a*=9.86 Å and *c*=15.25 Å. The image resolution was confirmed to be 1.6 Å by 0-60 reflection marked by a red circle in the FD of Fig 2A, and was among the highest spatial resolution ever achieved for any MOFs. This observation (and figs. S7 and S8) corroborates the preferential crystal orientation, (001)-AlFFIVE-1-Ni nanosheets. Symmetry averaged image of Fig 2A with *p*4*mmm* improved signal-to-noise ratio greatly and specified the atoms (Fig. 2B). Strong dark spots were observed with separation of ≈ 6.91 Å, consistent with the distance between adjacent inorganic extended chains (columns) formed by --F–Ni–F–Al–F-- (Fig. 2 C). Additionally, two weak dark elongated signals were also observed between the strong dark spots (separated by ≈ 1.9 Å), which can be attributed to a part of pyrazine, 2 carbon and 1 nitrogen atoms, acting as a linker between adjacent Ni(II).

Overcoming a big difficulty induced by the preferred orientation of nanosheets along the [001], high-resolution ABF images were taken with the [100] incidence, which is perpendicular to the [001] direction (Fig. 2D and fig. S9). Fig. 2D visualizes the square grid of Ni(II) and pyrazine pillared by $[AlF_5(H_2O)]^{2-}$, where the dark contrast is associated with Ni(II). The crystal structure of AlFFIVE-1-Ni along [100] direction matches well the corresponding experimental ABF image (Fig. 2E, and fig. S9). This in-depth STEM study confirms the successful synthesis of (001)-AlFFIVE-1-Ni nanosheets (hereafter as (001)-AlFFIVE or (001)-nanosheets) with excellent crystallinity and maximum exposure of 1D channels (Fig. 2F), which is a highly desirable morphology for achieving in-plane alignment of nanosheets in the polymer matrix.

Fabrication of [001]-oriented MMMOF membrane

It is of prime importance to in-plane align (001)-nanosheets in a polymer matrix to fabricate a uniform [001]-oriented/c-oriented MMMOF membrane and translate the 1D channel alignment from single nanosheets into a macroscopic continuous membrane for an efficient molecular separation (Fig. 3A). Commercially available state-of-the-art polyimide 6FDA-DAM, and lab synthesized 6FDA-DAM-DAT (1:1) and 6FDA-DAT polyimides were chosen as polymer matrices owing to their high thermal and

chemical stabilities, good mechanical strength, and excellent processability. We examined three different solvents ($CHCl_3$, THF, and DCM) as dispersant mediums to evaluate the effect of solvents for membrane fabrication and resultant CO_2/CH_4 separation. A solution-casting method was performed to fabricate pure polymeric and MMMOF membranes with a thickness of *ca*. 50–70 μm (supplementary method). The solvents effect in pure polymeric membranes was minimal. However, in MMMOF membrane, $CHCl_3$ presented higher CO_2/CH_4 selectivity followed by THF and DCM (fig. S10 and S11, and table S1). We evaluated nanosheets' dispersibility in different solvents and allow them to sediment, we noticed nanosheets begin sedimentation after 6~8 h in DCM, 22~25 h in THF, and no sedimentation in $CHCl_3$ even after 5 days. Thus, higher selectivity can be attributed to the better nanosheets dispersibility that prevents nanosheets sedimentation and/or agglomeration during membrane fabrication resultant homogeneous nanosheets alignment inside the polymer matrix.

The cross-section SEM images of 58.9 wt% nanosheets in 6FDA-DAM [(001)-AlFFIVE(*58.9*)/6FDA-DAM, parenthesis refer to MOF loading by wt%] reveal a uniform in-plane alignment of nanosheets in the polymer matrix (Fig. 3B and fig. S12). The focused ion beam SEM (FIB-SEM) images on an extensive area evidence that the majority of nanosheets are uniformly and in-plane aligned throughout the membrane (Fig. 3C, fig. S13, and Movie S2). These analyses also reveal an excellent nanosheets-polymer interface compatibility. XRD patterns of associated membrane (Fig. 3D) show only two major Bragg diffractions (indexed as the (002) and (004) crystallographic planes of AlFFIVE-1-Ni structure) corroborating the strong preferential in-plane alignment of (001)-nanosheets and the attainment of the desired uniform [001]-oriented MMMOF continuous membrane. These results demonstrate that the successful translation of single (001)-nanosheets into a [001]-oriented macroscopic membrane, where 1D channels of nanosheets are all parallel, an ideal scenario for distinct molecular separation (Fig. 3A).

Shear-flow or shear-force induced preferential alignment of 2D nanosheets within polymer matrix have been reported (*17, 30*). Here, (001)-nanosheets in-plane (*c*-axis) alignment is induced by a slow evaporation of solvent "slow evaporation-induced in-plane alignment of nanosheets" in the course of the membrane fabrication process. During slow solvent evaporation, nanosheets gradually self-arrange according to the minimum energy configuration (*31*)). The nanosheets concentration gradient and presence of the liquid-vapor interface may assists as a nucleating surface origins in-plane aligned nanosheets domains to grow gradually inward (Fig. 3E). If the solvent evaporation process is relatively fast, the nanosheets alignment may be kinetically affected and the final alignment may consolidate into a thermodynamically unfavored state (Fig. 3G) (*32*). In addition, solvent/(nanosheet+polymer) mass ratio

of 22-35 was found to be an optimal range for suitable in-plane alignment. Centrifugal force can also align nanosheets, accordingly [001]-oriented ultrathin membrane on porous α-Al_2O_3 support was prepared by spin coating method.

MOF loading, and associated properties of membranes were additionally analyzed by thermogravimetric analysis, Fourier transform infrared spectroscopy and XRD (figs. S14 to S16). We attained nanosheets loadings up to 59.9 wt% in 6FDA-DAM-DAT and 60.3 wt% in 6FDA-DAT, importantly, nanosheets loadings (up to 60 wt%) are remarkably high than isotropic fillers loadings (<35 wt%) (*10*). The ability to increase nanosheets loading offers an opportunity to closely mimic the associated pure MOF membrane, as well as to improve the separation performance of the membranes since the agglomeration, sedimentation, and random orientation of nanosheets within the polymer matrix is circumvented at high loadings. In the present case, no such adverse effects were observed (figs. S17 to S20).

Schematic illustrations of randomly oriented AlFFIVE-1-Ni nanoparticles embedded in polymer matrix is shown (Fig. 3H). The cross-section SEM image and XRD patterns of 37.1 wt% nanoparticles in 6FDA-DAM polymer showed a random orientation of the nanoparticles inside polymer matrix (Fig. 3, I and J, and fig. S21). Young's modulus and elongation strain of nanoparticles and nanosheets containing membranes were evaluated (Fig. 3K, and fig. S22). It was found that the incorporation of nanoparticles or nanosheets into polymer matrix results in an enhancement of Young's modulus and this enhancement was substantial in nanosheets containing membranes (Fig. 3K and table S3), which can be attributed to the better compatibility between nanosheets and polymer. Membranes fabricated using nanoparticles maintain good mechanical properties at relatively low MOF loading (26.3 wt%). Nanoparticle loadings up to 37.1 wt% were possible before the membrane became defective or too fragile to handle for gas separation studies. High loading (58.9 wt%) was possible using nanosheets (Fig. 3K, and fig. S22). Nanosheets proffered smooth and extended external surface area compared to nanoparticles, which promoted interactions with the polymer. The optimum nanosheets loading was found up to 64 wt%. Beyond this limit the resultant membrane was difficult to handle for gas separation studies due to its apparent fragility and plausible defects, resulting in relatively high permeability with lower selectivity.

We further endeavored to elucidate the enhanced interaction between nanosheets and polymer. The MOF-polymer suspension was prepared by stirring (250 rpm) at 35 °C for 2 h before membrane casting. We noticed MOF-polymer suspension became viscous and the relative viscosity change of nanosheets-polymer was considerably higher than that of nanoparticle-polymer suspension (Fig. 3L). The higher

viscosity of suspension implies the enhanced nanosheets-polymer interaction, possibly hydrogen bonding interaction between the imide groups of the 6FDA and the H of the pyrazine from (001)-nanosheets is plausibly providing better mechanical properties of nanosheet-incorporated membranes.

The gas separation performances of nanoparticles and (001)-nanosheets containing membranes were assessed under an equimolar CO_2/CH_4 mixture, and compared based on the volume and weight fraction (fig. S23). Regardless, the nanosheet membranes demonstrated substantially better separation. Even at similar MOF loading nanosheets offered higher permeability and selectivity (fig. S23). Nanoparticles always compensate permeability to gain selectivity that can be attributed to random orientation of nanoparticles with non-permeable (110) and (1-10) facets perpendicular to gas diffusion direction (Fig. 3I), ascertaining the importance of (001)-nanosheet morphology.

We also fabricated membrane using (001)-nanosheets in randomly aligned fashion and evaluated CO_2/CH_4 separation (fig. S24). The membrane presented high permeability but significantly reduced selectivity, presumably due to the presence of non-selective gas diffusion path associated to discontinuity of nanosheets staking as revealed by SEM images (Fig. 3G and fig. S24AB). This comparative study corroborates that in-plane alignment is essential to maximize membrane performance (fig. S24C).

We further evaluated how pore size/shape, and host-guest interactions are critical for concurrent enhancement of selectivity and permeability. Accordingly, we selected three MOFs affording their attainment as nanosheets morphology and with different pore system features. Ultra-small pore (~2.1 Å), $Zn_2(bim)_4$ nanosheets showed a negligible improvement in the selectivity associated with a substantial decrease in permeability. Relatively large pore (~6.2 Å), Zn-TCPP nanosheets showed higher permeability but associated with reduced selectivity (fig. S25). These results are in line with CO_2 adsorption isotherms of associated MOF nanosheets (fig. S25). Only (001)-AlFFIVE nanosheets MMMOF demonstrated a significant concurrent enhancement of selectivity and permeability.

The in silico constructed (001)-AlFFIVE/polymer composite model is illustrated (Fig. 3M and figs. S27 to 30). The top view reveals that polymer covers 1D channel of (001)-nanosheets (Fig. 3M), forming interlocked perpendicular pore zones. The side view confirms that the polymer remains at the MOF surface, thus no polymer penetration into the pores (fig. S27). We constructed a second nanosheet/6FDA-DAM composite model corresponding to a 42 wt% (001)-nanosheets loading in complement to the pristine one associated with a 59 wt% (001)-nanosheets loading (Fig. S27). The association of two components in the interfacial region is held by means of continued hydrogen bonding interactions with a nanosheets-polymer interface distances that ranges from 2.5 to 6.5 Å for both membranes (Fig. S27C and F). The so-

created interfacial region is characterized by the presence of interconnected pores from 2.5 to 4.0 Å size (fig. S29). This restricted dimension a priori prevents the gas to spread along the direction parallel to the nanosheets surface thus favoring straightforward pathways for the gas through the oriented 1D channel nanosheets/polymer, pinpointing to the importance of uniform [001]-oriented membranes for enhanced separation performance. Grand Canonical Monte Carlo (GCMC) simulations were performed to explore the CO_2 and CH_4 separation properties of the resulting membranes at 298 K. An analysis of the single-component (fig.S31) and binary mixture (Fig. 3N and fig. S31C) adsorption mechanism evidenced that CH_4 is almost exclusively adsorbed in the polymer phase while CO_2 equally populates the pores of the MOF and polymers (Fig.3N and fig. S31), confirming that nanosheets acts as a molecular barrier for CH_4. The interfacial region was found to be accessible to gas molecules, thus ensuring a connecting-path between the polymer and the oriented 1D MOF channel.

The impact of three interlocked criteria on gas separation properties

We conducted single gas permeation on [001]-oriented membranes and associated polymer membranes using 9 different gas molecules (fig. S32 and table S4). [001]-oriented membranes show higher CO_2 permeability as compared to its pure polymer membranes while their CH_4 permeability remain similar (Fig. 4A). This result corroborates a more effective transport of CO_2 via 1D channels of (001)-nanosheets that leads to the enhanced CO_2/CH_4 selectivity. It is a highly looked-for property in a particular MOF filler, allowing its deployment with various polymer matrices for concurrent enhancement of selectivity and permeability (fig. S32 and table S4).

Theoretical CO_2/CH_4 selectivity and CO_2 permeability of pure (001)-AlFFIVE-1-Ni membrane were 354 and 2035 barrer (back-calculated using Maxwell model). Experimentally obtained CO_2 permeability and CO_2/CH_4 selectivity of (001)-AlFFIVE/6FDA-DAM, (001)-AlFFIVE/6FDA-DAM-DAT, and (001)-AlFFIVE/6FDA-DAT membranes at different nanosheets loading are shown (Fig. 4B, and table S5). The in-plane aligned incorporation of nanosheets into the polymer matrix prompted a substantial increase in both CO_2 permeability and CO_2/CH_4 selectivity (Fig. 4B and table S5).

Single and mixed-gas separation studies under different CO_2 feed compositions (CO_2/CH_4: 10/90; 20/80 and 50/50) and feed pressure on [001]-oriented membranes and associated pure polymer membranes are shown (Fig. 4C and fig. S33 to S35). (001)-AlFFIVE/6FDA-DAM membrane exhibited a higher CO_2/CH_4 selectivity under mixed gas as compared to single gas feeds, in contrast to pure 6FDA-DAM (fig. S33B). Under mixed gas permeation, the preferential adsorption of CO_2 in nanosheets leads to remarkably reduced CH_4 permeability and therefore, enhanced CO_2/CH_4 selectivity (fig. S33D). (001)-

AlFFIVE/6FDA-DAM-DAT and (001)-AlFFIVE/6FDA-DAT membranes presented similar single and mixed gas selectivity (fig. S34D and S35D).

CO_2 concentration-dependent study revealed that mixed gas CO_2 permeability is similar to that of single gas permeability at a relatively high feed CO_2 concentration (CO_2/CH_4:50/50), nevertheless, CO_2 permeability gradually decreased as CO_2 feed concentration decreased to CO_2/CH_4 : 20/80 to 10/90 while selectivity was preserved (fig. S33D, S34D and S35D). CO_2 permeability decrease is highly likely due to the higher competition between CH_4 and CO_2. These results imply that CO_2/CH_4 separation at relatively low CO_2 concentration (CO_2/CH_4:20/80 and 10/90, typical CO_2 concentration in natural gas) is challenging but is of practical importance. Even under CO_2/CH_4:10/90 mixture, mixed gas CO_2 permeability improvement of 113% and 110%, and CO_2/CH_4 selectivity enhancement of 144% and 139% were achieved for (001)-AlFFIVE(*59.6*)/6FDA-DAM-DAT and (001)-AlFFIVE(*60.3*)/6FDA-DAT membranes, respectively, as compared to associated pure polymer membranes (Fig. 3C, fig. S34 and S35, and Tables S7 and S8). The enhanced separation corroborates the importance of judicious choice of MOF fillers and polymer pairs. These results also demonstrate that the relative enhancement of permeability and selectivity is pronounced in relatively low permeable polymer (table S6-8).

Temperature-dependent (20-100 °C) single and mixed-gas CO_2/CH_4 separation on [001]-oriented membranes and associated pure polymer membranes are shown (Fig. 4D and fig. S36 to S38). Increasing the permeation temperature significantly affects the CO_2/CH_4 separation. Particularly, both selectivity and permeability of pure polymeric membrane and nanoparticle membranes substantially deteriorated (Fig. 3D, fig. S36-S38). In contrast, in [001]-oriented membranes, the CO_2 permeability significantly increases with increasing temperature while retaining selectivity (fig. S36-S38). Likewise, we obtained variable temperature CO_2 adsorption isotherms on (001)-nanosheet powder (Fig. 1H). As the temperature increases the CO_2 adsorption lessens (weaker interactions). This decrease is pronounced for a temperature increase from 75 to 100 °C, prompting a significant enhancement of CO_2 permeability at relatively higher temperatures (Fig. S36-38). Notably, (001)-AlFFIVE/6FDA-DAM-DAT membrane demonstrated a drastic concurrent enhancement in CO_2 permeability of 355 % and CO_2/CH_4 selectivity of 470% compared to the pure 6FDA-DAM-DAT polymer even at 100 °C and under (CO_2/CH_4 : 20/80) separation (Fig. 4D and table S9 to S11). This CO_2/CH_4 separation at elevated temperature is the consequence of enhanced CO_2 diffusion via 1D channels of (001)-nanosheets, uniform in-plane alignment of nanosheets and remarkably high nanosheets loading.

We deconvoluted CO_2 and CH_4 permeability into diffusion coefficient (diffusivity, D_i) and sorption coefficient (solubility, S_i) based on the solution-diffusion model (*33*). By changing permeation temperature membranes exhibited opposite propensity of solubility and diffusivity of the gases (CO_2 and CH_4). Specifically, increasing the temperature considerably decreases CO_2 and CH_4 solubility but substantially increases CO_2 diffusivity in both membranes (fig. S39 A and B). The (001)-AlFFIVE/6FDA-DAM-DAT membrane demonstrated a significant enhancement in CO_2 diffusivity but a sharp decrease in CH_4 diffusivity, compared to 6FDA-DAM-DAT (fig. S39, A and B and table S12), affording a diffusion dominated with exceptionally high CO_2/CH_4 separation in a wide range of temperatures (Fig. 5E, and fig.S39C). We measured membrane stability under thermal stress, (001)-AlFFIVE/6FDA-DAM-DAT membrane demonstrated excellent reversibility in CO_2 permeability and CO_2/CH_4 selectivity in a wide range of temperature and a duration of least 400 h (Fig. 4F).

A comparison of CO_2/CH_4 separation performance of [001]-oriented membranes with other reported MOF-nanoparticles/6FDA-polyimides membranes is presented in Fig. 4G and tables S13 to S15. It is clear from Fig. 5G that the performance of the [001]-oriented membranes reported here exceeds that of others reported in the literature. More appropriate comparison with MOF-nanosheets/polymer membranes attests to the superior performance of [001]-oriented membranes (fig. S40 and table S14) (*17, 18, 34, 35*). The CO_2/CH_4 separation on ultrathin [001]-oriented membrane on porous α-Al_2O_3 supports was assessed. Preliminary results exhibited an 11 fold increase of CO_2 permeance than thick membrane and selectivity was preserved (fig. S41). Although better separation performances have been reported for thin supported zeolite and carbon molecular sieve membrane films (*36*), this family of MMMOF membranes have a straightforward manufacture process, excellent mechanical properties and stability to stream, with no signs of plasticization were observed for more than 30 days,

As CO_2/CH_4 separation at relatively low CO_2 concentrations (10%) is more challenging than that of high concentration (50%), the latter concentration is typically analyzed for study purposes (Table S15). Importantly, [001]-oriented membranes demonstrated outstanding separation at relatively low CO_2 concentration. Correspondingly, we dedicated our gas separation to the ternary mixture under realistic row natural gas composition ($H_2S/CO_2/CH_4$: 1/9/90; 2/18/80 and 5/5/90) (*37*). For natural gas purification, both CO_2 and H_2S must be removed from CH_4, hence the acid gas removal performance can be evaluated by measuring the total acid gas permeability [$P(CO_2)$ + $P(H_2S)$] and selectivity [$P(CO_2)$ + $P(H_2S)$]/$P(CH_4)$](*12*). Even under $H_2S/CO_2/CH_4$:1/9/90 mixture, the mixed gas (H_2S + CO_2) permeability improvement of 63%, 104% and 140%, and (H_2S+CO_2)/CH_4 selectivity enhancement of 123%, 112% and

103% were achieved for the (001)-AlFFIVE(*58.9*)/6FDA-DAM, (001)-AlFFIVE(*59.6*)/6FDA-DAM-DAT and (001)-AlFFIVE(*60.3*)/6FDA-DAT membranes, respectively, compared to the associated pure polymer membranes (Table S16). AlFFIVE-1-Ni has a similar adsorption selectivity (H_2S/CO_2 selectivity close to 1), therefore it is capable of removing both gases simultaneously (*26*). We have demonstrated an adsorbent separation selectivity can be translated into the processable matrix.

The comparative study reveals that the performance of the [001]-oriented membranes reported here exceeds that of others reported in the literature (Fig. 4H) (*38, 39*). The performance stability of membrane under continuously mixed gas permeation conditions is a critical test to assess the membrane longevity and the reproducibility of its associated properties. Direct application of our best-performing membranes to a 1/9/90:$H_2S/CO_2/CH_4$ mixture leads to 6/85/09:$H_2S/CO_2/CH_4$ mixture in permeate site at least 30 days of continuous operation (fig. S42).

We further evaluated the separation performance of [001]-oriented membranes under high feed pressure that reflects practical natural gas purification (*40*). Membrane permeation was studied under high feed pressures up to 35 bar (Fig. 4I and fig. S43). Importantly, no abrupt selectivity and/or permeability loss occurred in the [001]-oriented membranes for the total acidic gas removal even under 35 bar pressure (fig. S43 and S44).

The separation performances of oriented membranes were further tested for other gas pairs, including H_2/N_2, H_2/CH_4 and H_2/C_3H_8 and subsequently compared with the literature (*3*) in fig. S45. The resultant membranes exhibited excellent selectivity and permeability enhancement for these gas pairs, far beyond the upper-bounds for polymeric membranes.

Conclusions

The enhanced performances reported here can be rationalized by recognizing the importance of three essential criteria described earlier. The attainment of in-plane alignment and extremely high loading of (001)-nanosheets is distinctively responsible for the achieved separation performance. Nanosheets selectively transporting gases based on their kinetic diameter through the oriented membranes. In fact, this centimeter-scale flexible [001]-oriented membrane can be regarded as a single piece of a flexible crystal where thousands of nanosheets are uniformly aligned in a predefined crystallographic direction, and the gaps between aligned nanosheets are filled with polymer. The results confirm the potential of tailoring MOF crystal morphology into oriented nanosheets, allowing the desired orientation of the 1D channels parallel to the gas diffusion direction and proffering opportunities to maximize the performance of the oriented membrane as demonstrated here for various gas separations.

REFERENCES AND NOTES

1. U.S. Department of Energy. Materials for separation technologies: energy and emission reduction opportunities. DOI : 10.2172/1218755 (2005).
2. D. S. Sholl, R. P. Lively, Seven chemical separations to change the world. *Nature* **532**, 435-437 (2016).
3. L. M. Robeson, The upper bound revisited. *J. Membr. Sci.* **320**, 390-400 (2008).
4. D. L. Gin, R. D. Noble, Designing the next generation of chemical separation membranes. *Science* **332**, 674-676 (2011).
5. W. J. Koros, C. Zhang, Materials for next-generation molecularly selective synthetic membranes. *Nat. Mater.* **16**, 289-297 (2017).
6. J. Dechnik, J. Gascon, C. J. Doonan, C. Janiak, C. J. Sumby, Mixed-matrix membranes. *Angew. Chem. Int. Ed.* **56**, 9292-9310 (2017).
7. B. Seoane *et al.*, Metal-organic framework based mixed matrix membranes: a solution for highly efficient CO_2 capture? *Chem. Soc. Rev.* **44**, 2421-2454 (2015).
8. G. Dong, H. Li, V. Chen, Challenges and opportunities for mixed-matrix membranes for gas separation. *J. Mater. Chem. A.* **1**, 4610–4630 (2013).
9. Y. Cheng *et al.*, Advanced porous materials in mixed matrix membranes. *Adv. Mater.* **30**, 1802401 (2018).
10. J. Dechnik, C. J. Sumby, C. Janiak, Enhancing mixed-matrix membrane performance with metal–organic framework additives. *Cryst. Growth Des.* **17**, 4467-4488 (2017).
11. G. Liu *et al.*, Mixed matrix formulations with MOF molecular sieving for key energy-intensive separations. *Nat. Mater.* **17**, 283-289 (2018).
12. J. Sánchez-Laínez *et al.*, Influence of ZIF-8 particle size in the performance of polybenzimidazole mixed matrix membranes for pre-combustion CO_2 capture and its validation through interlaboratory test. *J. Membr. Sci.* **515**, 45-53 (2016).
13. A. Sabetghadam *et al.*, Metal organic framework crystals in mixed-matrix membranes: impact of the filler morphology on the gas separation performance. *Adv. Funct. Mater.* **26**, 3154-3163 (2016).
14. B. Ghalei *et al.*, Enhanced selectivity in mixed matrix membranes for CO_2 capture through efficient dispersion of amine-functionalized MOF nanoparticles. *Nat. Energy* **2**, 17086 (2017).
15. A. Knebel *et al.*, Solution processable metal-organic frameworks for mixed matrix membranes using porous liquids. *Nat. Mater.* **19**, 1346-1353 (2020).
16. H. B. Park, J. Kamcev, L. M. Robeson, M. Elimelech, B. D. Freeman, Maximizing the right stuff: the trade-off between membrane permeability and selectivity. *Science* **356**, eaab0530 (2017).
17. T. Rodenas *et al.*, Metal-organic framework nanosheets in polymer composite materials for gas separation. *Nat. Mater.* **14**, 48-55 (2015).
18. A. Pustovarenko *et al.*, Nanosheets of nonlayered aluminum metal-organic frameworks through a surfactant-assisted method. *Adv. Mater.* **30**, 1707234 (2018).
19. X. Li, J. Hou, R. Guo, Z. Wang, J. Zhang, Constructing unique cross-sectional structured mixed matrix membranes by incorporating ultrathin microporous nanosheets for efficient CO_2 separation. *ACS Appl. Mater. Interfaces* **11**, 24618-24626 (2019).
20. Y. Cheng *et al.*, Enhanced polymer crystallinity in mixed-matrix membranes induced by metal-organic framework nanosheets for efficient CO_2 capture. *ACS Appl. Mater. Interfaces* **10**, 43095-43103 (2018).
21. C. Li, C. Wu, B. Zhang, Enhanced CO_2/CH_4 separation performances of mixed matrix membranes incorporated with two-dimensional Ni-based MOF nanosheets. *ACS Sustain. Chem. Eng.* **8**, 642-648 (2019).
22. O. Kwon *et al.*, High-aspect ratio zeolitic imidazolate framework (ZIF) nanoplates for hydrocarbon separation membranes. *Sci. Adv.* **8**, eabl6841 (2022).

23. P. M. Bhatt, V. Guillerm, S. J. Datta, A. Shkurenko, M. Eddaoudi, Topology meets reticular chemistry for chemical separations: MOFs as a case study. *Chem* **6**, 1613-1633 (2020).
24. Y.-z. Li, Z.-h. Fu, G. Xu, Metal-organic framework nanosheets: preparation and applications. *Coord. Chem. Rev.* **388**, 79-106 (2019).
25. A. Cadiau *et al.*, Hydrolytically stable fluorinated metal-organic frameworks for energy-efficient dehydration. *Science* **356**, 731-735 (2017).
26. Y. Belmabkhout *et al.*, Natural gas upgrading using a fluorinated MOF with tuned H_2S and CO_2 adsorption selectivity. *Nat. Energy* **3**, 1059-1066 (2018).
27. M. Zhao *et al.*, Two-dimensional metal-organic framework nanosheets: synthesis and applications. *Chem. Soc. Rev.* **47**, 6267-6295 (2018).
28. L. Zhuang *et al.*, A surfactant-free and scalable general strategy for synthesizing ultrathin two-dimensional metal-organic framework nanosheets for the oxygen evolution reaction. *Angew. Chem. Int. Ed.* **58**, 13565-13572 (2019).
29. S. Zhao *et al.*, Ultrathin metal–organic framework nanosheets for electrocatalytic oxygen evolution. *Nat. Energy* **1**, (2016).
30. C. Zhao *et al.*, Layered nanocomposites by shear-flow-induced alignment of nanosheets. *Nature* **580**, 210-215 (2020).
31. C. J. Brinker, Y. Lu, A. Sellinger, H. Fan, Evaporation-induced self-assembly: nanostructures made easy. *Adv. Mater.* **11**, 579-585 (1999).
32. Y. Zhu *et al.*, Evaporation-induced vertical alignment enabling directional ion transport in a 2D-nanosheet-based battery electrode. *Adv. Mater.* **32**, 1907941 (2020).
33. J. G. Wijmans, R. W. Baker, The solution-diffusion model: a review. *J. Membr. Sci.* **107**, 1-21 (1995).
34. Y. Yang, K. Goh, R. Wang, T. H. Bae, High-performance nanocomposite membranes realized by efficient molecular sieving with CuBDC nanosheets. *Chem. Commun.* **53**, 4254-4257 (2017).
35. M. Shete *et al.*, On the direct synthesis of Cu(BDC) MOF nanosheets and their performance in mixed matrix membranes. *J. Membr. Sci.* **549**, 312-320 (2018).
36. D. D. Iarikov, S. T. Oyama. (Review of CO_2/CH_4 separation membranes, in Membrane Science and Technology, Elsevier, 2011), vol. 14, pp. 91-115.
37. M. A. Al-Saleh, S. O. Duffuaa, M. A. Al-Marhoun, J. A. Al-Zayer, Impact of crude oil production on the petrochemical industry in Saudi Arabia. *Energy* **16**, 1089-1099 (1991).
38. G. Liu *et al.*, Enabling fluorinated MOF-based membranes for simultaneous removal of H_2S and CO_2 from natural gas. *Angew. Chem. Int. Ed.* **57**, 14811-14816 (2018).
39. M. Z. Ahmad *et al.*, High-pressure CO_2/CH_4 separation of Zr-MOFs based mixed matrix membranes. *Sep. Purif. Technol.* **230**, 115858 (2020).
40. R. W. Baker, K. Lokhandwala, Natural gas processing with membranes: an overview. *Ind. Eng. Chem. Res.* **47**, 2109-2121 (2008).
41. G. Liu *et al.*, Zeolite-like MOF nanocrystals incorporated 6FDA-polyimide mixed-matrix membranes for CO_2/CH_4 separation. *J. Membr. Sci.* **565**, 186-193 (2018).
42. Y. Liu *et al.*, Enhanced CO_2/CH_4 separation performance of a mixed matrix membrane based on tailored MOF-polymer formulations. *Adv. Sci.* **5**, 1800982 (2018).
43. T. H. Bae *et al.*, A high-performance gas-separation membrane containing submicrometer-sized metal-organic framework crystals. *Angew. Chem. Int. Ed.* **49**, 9863–9866 (2010).
44. J. E. Bachman, J. R. Long, Plasticization-resistant Ni_2(dobdc)/polyimide composite membranes for the removal of CO_2 from natural gas. *Energy Environ. Sci.* **9**, 2031-2036 (2016).
45. M. Askari, T.-S. Chung, Natural gas purification and olefin/paraffin separation using thermal cross-linkable co-polyimide/ZIF-8 mixed matrix membranes. *J. Membr. Sci.* **444**, 173-183 (2013).
46. Y. Peng, Y. Li, Y. Ban, W. Yang, Two-dimensional metal-organic framework nanosheets for membrane-based gas separation. *Angew. Chem. Int. Ed.* **56**, 9757-9761 (2017).

47. B. Wang *et al.*, General approach to metal-organic framework nanosheets with controllable thickness by using metal hydroxides as precursors. *Front. Mater.* **7**, 37 (2020).
48. W. Qiu, L. Xu, C.-C. Chen, D. R. Paul, W. J. Koros, Gas separation performance of 6FDA-based polyimides with different chemical structures. *Polymer* **54**, 6226-6235 (2013).
49. L. Wang, Y. Cao, M. Zhou, S. J. Zhou, Q. Yuan, Novel copolyimide membranes for gas separation. *J. Membr. Sci.* **305**, 338-346 (2007).
50. B. Kraftschik, W. J. Koros, J. R. Johnson, O. Karvan, Dense film polyimide membranes for aggressive sour gas feed separations. *J. Membr. Sci.* **428**, 608-619 (2013).
51. C. T. Koch, Determination of core structure periodicity and point defect density along dislocations, Arizona State University, Ann Arbor (2002).
52. G. Kresse, J. Furthmüller, Efficient iterative schemes for ab initio total-energy calculations using a plane-wave basis set. *Phys. Rev. B Condens. Matter* **54**, 11169-11186 (1996).
53. P. E. Blochl, Projector augmented-wave method. *Phys. Rev. B Condens. Matter* **50**, 17953-17979 (1994).
54. J. P. Perdew, K. Burke, M. Ernzerhof, Generalized gradient approximation made simple. *Phys. Rev. Lett.* **77**, 3865-3868 (1996).
55. S. Grimme, J. Antony, S. Ehrlich, H. Krieg, A consistent and accurate ab initio parametrization of density functional dispersion correction (DFT-D) for the 94 elements H-Pu. *J. Chem. Phys.* **132**, 154104 (2010).
56. L. Wang, T. Maxisch, G. Ceder, Oxidation energies of transition metal oxides within the GGA+U framework. *Phys. Rev. B* **73**, 195107 (2006).
57. G. Makov, M. C. Payne, Periodic boundary conditions in ab initio calculations. *Phys. Rev. B Condens. Matter* **51**, 4014-4022 (1995).
58. T. A. Manz, D. S. Sholl, Improved atoms-in-molecule charge partitioning functional for simultaneously reproducing the electrostatic potential and chemical states in periodic and nonperiodic materials. *J. Chem. Theory. Comput.* **8**, 2844-2867 (2012).
59. A. K. Rappe, C. J. Casewit, K. S. Colwell, W. A. Goddard, W. M. Skiff, UFF, a full periodic table force field for molecular mechanics and molecular dynamics simulations. *J. Am. Chem. Soc.* **114**, 10024-10035 (1992).
60. S. L. Mayo, B. D. Olafson, W. A. Goddard, DREIDING: a generic force field for molecular simulations. *J. Phys. Chem.* **94**, 8897-8909 (1990).
61. S. Hwang *et al.*, Revealing the transient concentration of CO_2 in a mixed-matrix membrane by IR microimaging and molecular modeling. *Angew. Chem. Int. Ed.* **57**, 5156-5160 (2018).
62. S. Plimpton, Fast parallel algorithms for short-range molecular dynamics. *J. Comput. Phys.* **117**, 1-19 (1995).
63. L. J. Abbott, K. E. Hart, C. M. Colina, Polymatic: a generalized simulated polymerization algorithm for amorphous polymers. *Theor. Chem. Acc.* **132**, 1334 (2013).
64. M. Z. Ahmad *et al.*, Enhanced gas separation performance of 6FDA-DAM based mixed matrix membranes by incorporating MOF UiO-66 and its derivatives. *J. Membr. Sci.* **558**, 64-77 (2018).
65. I. T. Todorov, W. Smith, K. Trachenko, M. T. Dove, DL_POLY_3: new dimensions in molecular dynamics simulations via massive parallelism. *J. Mater. Chem.* **16**, 1911–1918 (2006).
66. P. P. Ewald, Die berechnung optischer und elektrostatischer gitterpotentiale. *Ann. Phys.* **369**, 253-287 (1921).
67. D. Dubbeldam, S. Calero, D. E. Ellis, R. Q. Snurr, RASPA: molecular simulation software for adsorption and diffusion in flexible nanoporous materials. *Mol Simul* **42**, 81-101 (2015).
68. J. G. Harris, K. H. Yung, Carbon dioxide's liquid-vapor coexistence curve and critical properties as predicted by a simple molecular model. *J. Phys. Chem.* **99**, 12021-12024 (1995).
69. M. G. Martin, J. I. Siepmann, Transferable potentials for phase equilibria. 1. united-atom description of n-alkanes. *J. Phys. Chem. B* **102**, 2569-2577 (1998).

70. T. J. H. Vlugt, E. García-Pérez, D. Dubbeldam, S. Ban, S. Calero, Computing the heat of adsorption using molecular simulations: the effect of strong coulombic interactions. *J. Chem. Theory Comput.* **4**, 1107-1118 (2008).
71. G. Yu *et al.*, Constructing connected paths between UiO-66 and PIM-1 to improve membrane CO_2 separation with crystal-like gas selectivity. *Adv. Mater.* **31**, 1806853 (2019).
72. K. Chen *et al.*, Enhanced CO_2/CH_4 separation performance of mixed-matrix membranes through dispersion of sorption-selective MOF nanocrystals. *J. Membr. Sci.* **563**, 360-370 (2018).
73. H. Gong, C. Y. Chuah, Y. Yang, T.-H. Bae, High performance composite membranes comprising $Zn(pyrz)_2(SiF_6)$ nanocrystals for CO_2/CH_4 separation. *Ind. Eng. Chem. Res.* **60**, 279-285 (2018).
74. H. Wang, S. He, X. Qin, C. Li, T. Li, Interfacial engineering in metal-organic framework-based mixed matrix membranes using covalently grafted polyimide brushes. *J. Am. Chem. Soc.* **140**, 17203-17210 (2018).
75. Q. Xin *et al.*, Mixed matrix membranes composed of sulfonated poly(ether ether ketone) and a sulfonated metal–organic framework for gas separation. *J. Membr. Sci.* **488**, 67-78 (2015).
76. X. Ma, X. Wu, J. Caro, A. Huang, Polymer composite membrane with penetrating ZIF-7 sheets displays high hydrogen permselectivity. *Angew. Chem. Int. Ed.* **58**, 16156-16160 (2019).
77. N. Tien-Binh, H. Vinh-Thang, X. Y. Chen, D. Rodrigue, S. Kaliaguine, Crosslinked MOF-polymer to enhance gas separation of mixed matrix membranes. *J. Membr. Sci.* **520**, 941-950 (2016).
78. O. G. Nik, X. Y. Chen, S. Kaliaguine, Functionalized metal organic framework-polyimide mixed matrix membranes for CO_2/CH_4 separation. *J. Membr. Sci.* **413-414**, 48-61 (2012).
79. M. R. Khdhayyer *et al.*, Mixed matrix membranes based on UiO-66 MOFs in the polymer of intrinsic microporosity PIM-1. *Sep. Purif. Technol.* **173**, 304-313 (2017).
80. N. Tien-Binh, H. Vinh-Thang, X. Y. Chen, D. Rodrigue, S. Kaliaguine, Polymer functionalization to enhance interface quality of mixed matrix membranes for high CO_2/CH_4 gas separation. *J. Mater. Chem. A* **3**, 15202-15213 (2015).
81. F. Dorosti, M. Omidkhah, R. Abedini, Fabrication and characterization of Matrimid/MIL-53 mixed matrix membrane for CO_2/CH_4 separation. *Chem. Eng. Res. Des.* **92**, 2439-2448 (2014).
82. X. Y. Chen, V.-T. Hoang, D. Rodrigue, S. Kaliaguine, Optimization of continuous phase in amino-functionalized metal–organic framework (MIL-53) based co-polyimide mixed matrix membranes for CO_2/CH_4 separation. *RSC Adv.* **3**, 24266–24279 (2013).
83. X. Guo *et al.*, Mixed matrix membranes incorporated with amine-functionalized titanium-based metal-organic framework for CO_2/CH_4 separation. *J. Membr. Sci.* **478**, 130-139 (2015).
84. M. Waqas Anjum, B. Bueken, D. De Vos, I. F. J. Vankelecom, MIL-125(Ti) based mixed matrix membranes for CO_2 separation from CH_4 and N_2. *J. Membr. Sci.* **502**, 21-28 (2016).
85. A. Kılıç, Ç. Atalay-Oral, A. Sirkecioğlu, Ş. B. Tantekin-Ersolmaz, M. G. Ahunbay, Sod-ZMOF/Matrimid® mixed matrix membranes for CO_2 separation. *J. Membr. Sci.* **489**, 81-89 (2015).
86. T. Li, Y. Pan, K.-V. Peinemann, Z. Lai, Carbon dioxide selective mixed matrix composite membrane containing ZIF-7 nano-fillers. *J. Membr. Sci.* **425-426**, 235-242 (2013).
87. N. A. H. M. Nordin, A. F. Ismail, A. Mustafa, R. S. Murali, T. Matsuura, The impact of ZIF-8 particle size and heat treatment on CO_2/CH_4 separation using asymmetric mixed matrix membrane. *RSC Adv.* **4**, 52530-52541 (2014).
88. S. Shahid *et al.*, MOF-mixed matrix membranes: precise dispersion of MOF particles with better compatibility via a particle fusion approach for enhanced gas separation properties. *J. Membr. Sci.* **492**, 21-31 (2015).
89. M. J. C. Ordoñez, K. J. Balkus, J. P. Ferraris, I. H. Musselman, Molecular sieving realized with ZIF-8/Matrimid® mixed-matrix membranes. *J. Membr. Sci.* **361**, 28-37 (2010).
90. A. F. Bushell *et al.*, Gas permeation parameters of mixed matrix membranes based on the polymer of intrinsic microporosity PIM-1 and the zeolitic imidazolate framework ZIF-8. *J. Membr. Sci.* **427**, 48-62 (2013).

91. S. N. Wijenayake *et al.*, Surface cross-linking of ZIF-8/polyimide mixed matrix membranes (MMMs) for gas separation. *Ind. Eng. Chem. Res.* **52**, 6991-7001 (2013).
92. S. Japip, H. Wang, Y. Xiao, T.-S. Chung, Highly permeable zeolitic imidazolate framework (ZIF)-71 nano-particles enhanced polyimide membranes for gas separation. *J. Membr. Sci.* **467**, 162-174 (2014).
93. S. Shahid, K. Nijmeijer, Performance and plasticization behavior of polymer–MOF membranes for gas separation at elevated pressures. *J. Membr. Sci.* **470**, 166-177 (2014).
94. E. A. Feijani, H. Mahdavi, A. Tavasoli, Poly(vinylidene fluoride) based mixed matrix membranes comprising metal organic frameworks for gas separation applications. *Chem. Eng. Res. Des.* **96**, 87-102 (2015).
95. C. Duan, X. Jie, D. Liu, Y. Cao, Q. Yuan, Post-treatment effect on gas separation property of mixed matrix membranes containing metal organic frameworks. *J. Membr. Sci.* **466**, 92-102 (2014).
96. H. Ren, J. Jin, J. Hu, H. Liu, Affinity between metal–organic frameworks and polyimides in asymmetric mixed matrix membranes for gas separations. *Ind. Eng. Chem. Res.* **51**, 10156-10164 (2012).
97. E. V. Perez, K. J. Balkus, J. P. Ferraris, I. H. Musselman, Mixed-matrix membranes containing MOF-5 for gas separations. *J. Membr. Sci.* **328**, 165-173 (2009).
98. H. B. Tanh Jeazet *et al.*, Increased selectivity in CO_2/CH_4 separation with mixed-matrix membranes of polysulfone and mixed-MOFs MIL-101(Cr) and ZIF-8. *Eur. J. Inorg. Chem.*, 4363-4367 (2016).
99. T. Rodenas, M. van Dalen, P. Serra-Crespo, F. Kapteijn, J. Gascon, Mixed matrix membranes based on NH_2-functionalized MIL-type MOFs: influence of structural and operational parameters on the CO_2/CH_4 separation performance. *Microporous Mesoporous Mater.* **192**, 35-42 (2014).

Acknowledgements

Funding: This research was supported by King Abdullah University of Science and Technology (KAUST). S.J.D. and M.E. acknowledge supports from KAUST. O.T. acknowledge supports from *CħEM*, ShanghaiTech Universithy (#EM02161943). A.M. acknowledges the Spanish Ministry of Science and Innovation (RYC2018-024561-I), Regional government of Aragon (DGA E13_20R). **Author contributions:** S.J.D. and M.E. conceived the idea of the project, designed experiments and wrote manuscript. S.J.D. synthesized MOF nanosheets, optimized, fabricated and characterized the membranes, and analyzed the data. P.M.B. performed gas adsorption isotherms. A.M. and O.T. contributed crystallographic aspect through STEM analysis. N.M.S.B., S.J.D. and M.K. obtained gas permeation study. I.D.C. synthesized polymers. D.F., P.G.M., R.S. and G.M. performed molecular simulations. All authors contributed to revising the manuscript. **Competing interest**: M.E. and S.J.D. has filed a patent with the USPTO serial no. 63/328,427. **Data and materials availability:** All data are available in the manuscript or the supplementary materials.

SUPPLEMENTARY MATERIALS

www.sciencemag.org/content/XXX
Materials and Methods
Supplementary Text
Figs. S1 to S47
Tables S1 to S20
References (*41*-*99*)
Movies S1 and S2

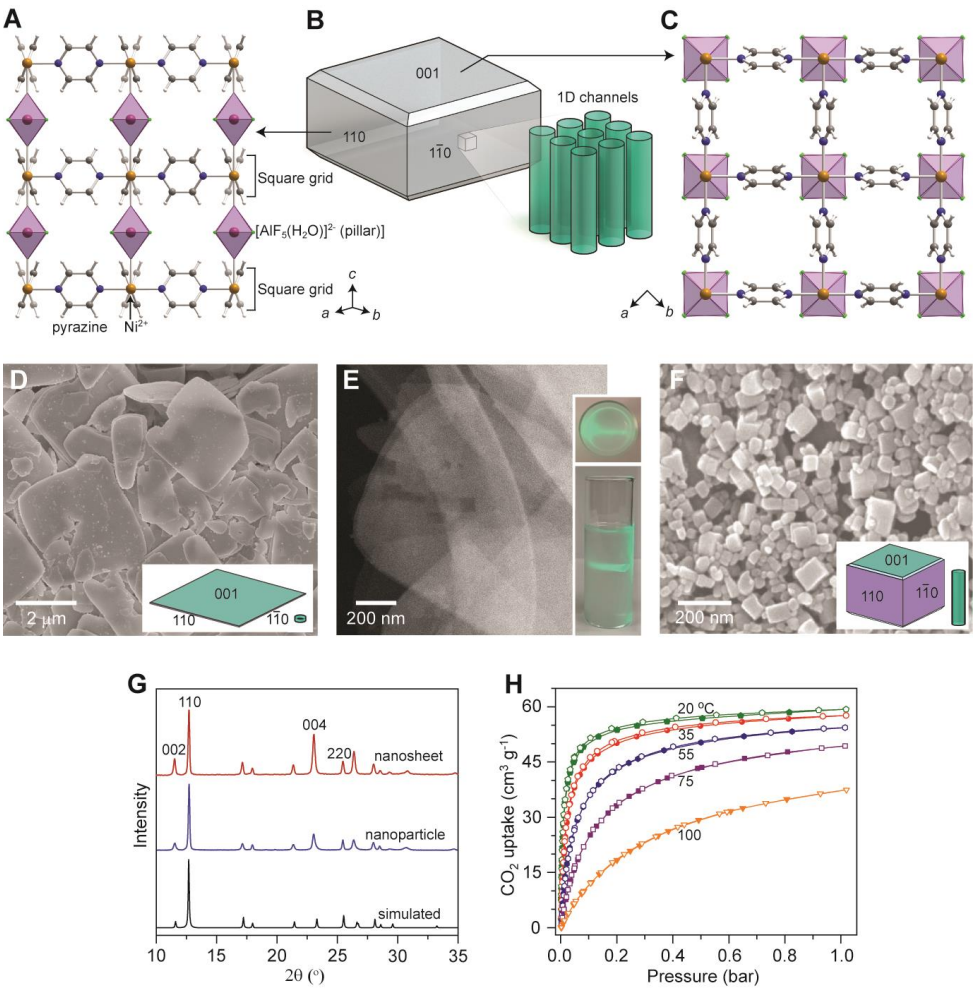

Fig. 1. Crystal structure and morphology of AlFFIVE-1-Ni (point group 4/*mmm*). (**A**) Structure view along [110 or 1-10] direction. (**B**) Schematic illustration of truncated bipyramidal morphology and 1D channel orientation. (**C**) Structure view along the [001] direction. (**D**) SEM image of nanosheets. Inset: large 001 surface and short channel. (**E**) Low-resolution STEM image of nanosheets. Inset: photos showing Tyndall effect on nanosheets, using a green laser. (**F**) SEM image of nanoparticles. Inset: depicted crystal morphology and long channel. (**G**) Powder XRD patterns (λ= 1.54056 Å) of nanosheets and nanoparticles. (**H**) CO_2 adsorption isotherms of nanosheets between 20 to 100 ºC.

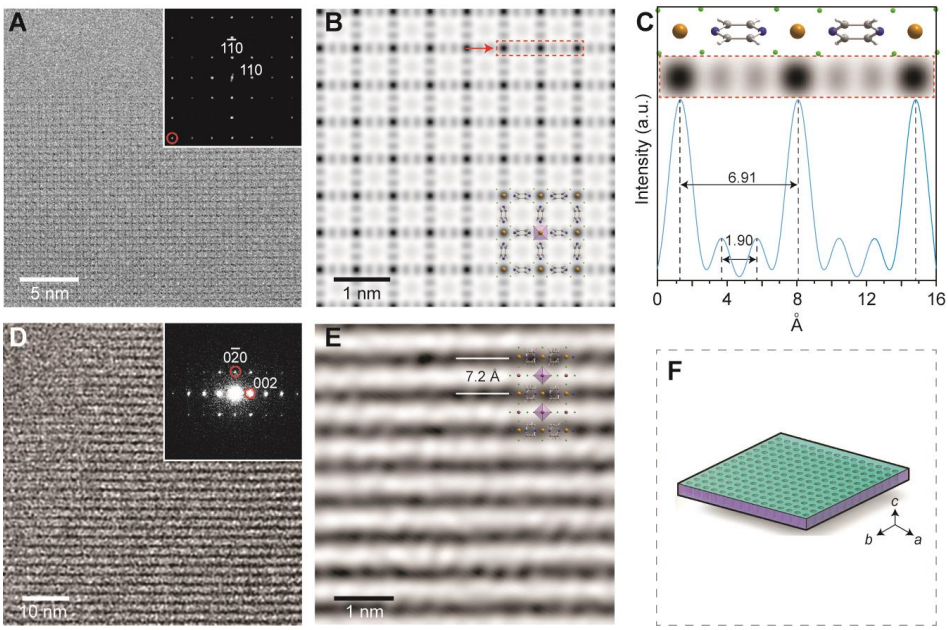

Fig. 2. C_s-corrected STEM images of AlFFIVE-1-Ni nanosheets acquired from different zone axes. (**A**) An annular bright-field (ABF) image along [001] with the Fourier diffractogram (FD). (**B**) Symmetry averaged image of (A) and an overlaid crystal structure. (**C**) Enlarged a part marked by the dotted red rectangle and intensity profile along the red arrow of (B), and associated structure model. (**D**) ABF image taken with [100] incidence. (**E**) Wiener filtered image with superimposed atomic structure. Color code: Ni(II) orange, Al(III) purple, C gray, F green, N blue. (**F**) Schematic illustration of nanosheet with 1D channel orientation.

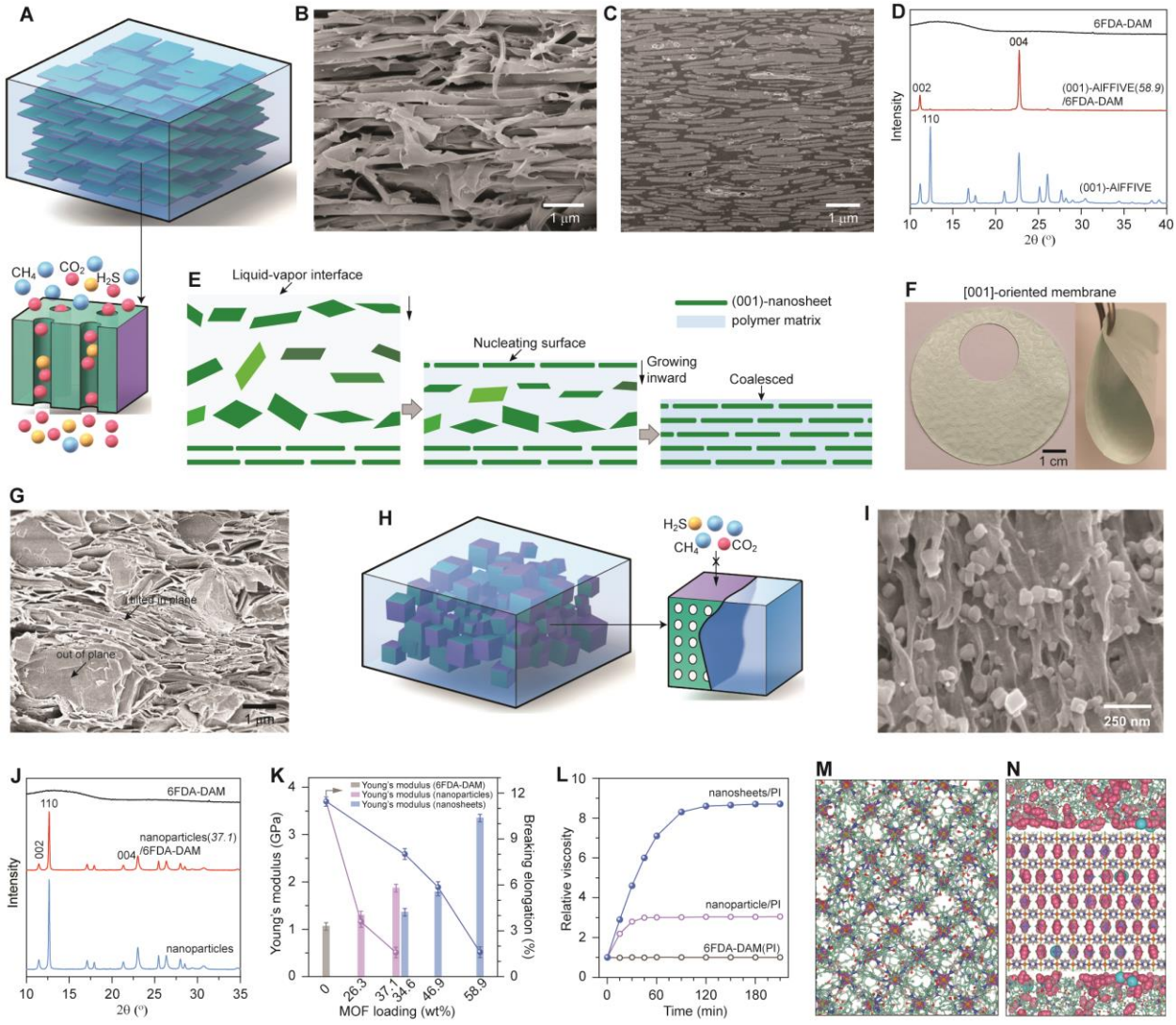

Fig. 3. Fabrication and characterization of [001]-oriented MMMOF membranes. (**A**) Schematic illustration of [001]-oriented membrane and an efficient H_2S and CO_2 separation process through 1D channel. (**B** and **C**) Cross-section SEM image (B) and FIB-SEM image (C) of (001)-AlFFIVE(*58.9*)/6FDA-DAM membrane. (**D**) XRD patterns of [001]-oriented membrane and nanosheet crystallite. (**E**) Illustration of 'slow evaporation-induced in-plane alignment' of nanosheets in polymer matrix. (**F**) Photographs of membrane. (**G**) Cross-section SEM image of random fashion nanosheets membrane. (**H**) Illustration of random fashion nanoparticles embedded in polymer matrix. (**I** and **J**) Cross-section SEM image (I) and XRD pattern (J) of nanoparticle(*37.1*)/6FDA-DAM membrane. (**K**) Mechanical studies of the membranes. (**L**) Relative viscosity changes of MOF/polymer and polymer suspension. (**M** and **N**) Computational studies of [001]-oriented membrane. Color code: polymer phase (transparent sky blue), MOF in (001)-facet (green) and (110)- or (1-10)-facet (purple).

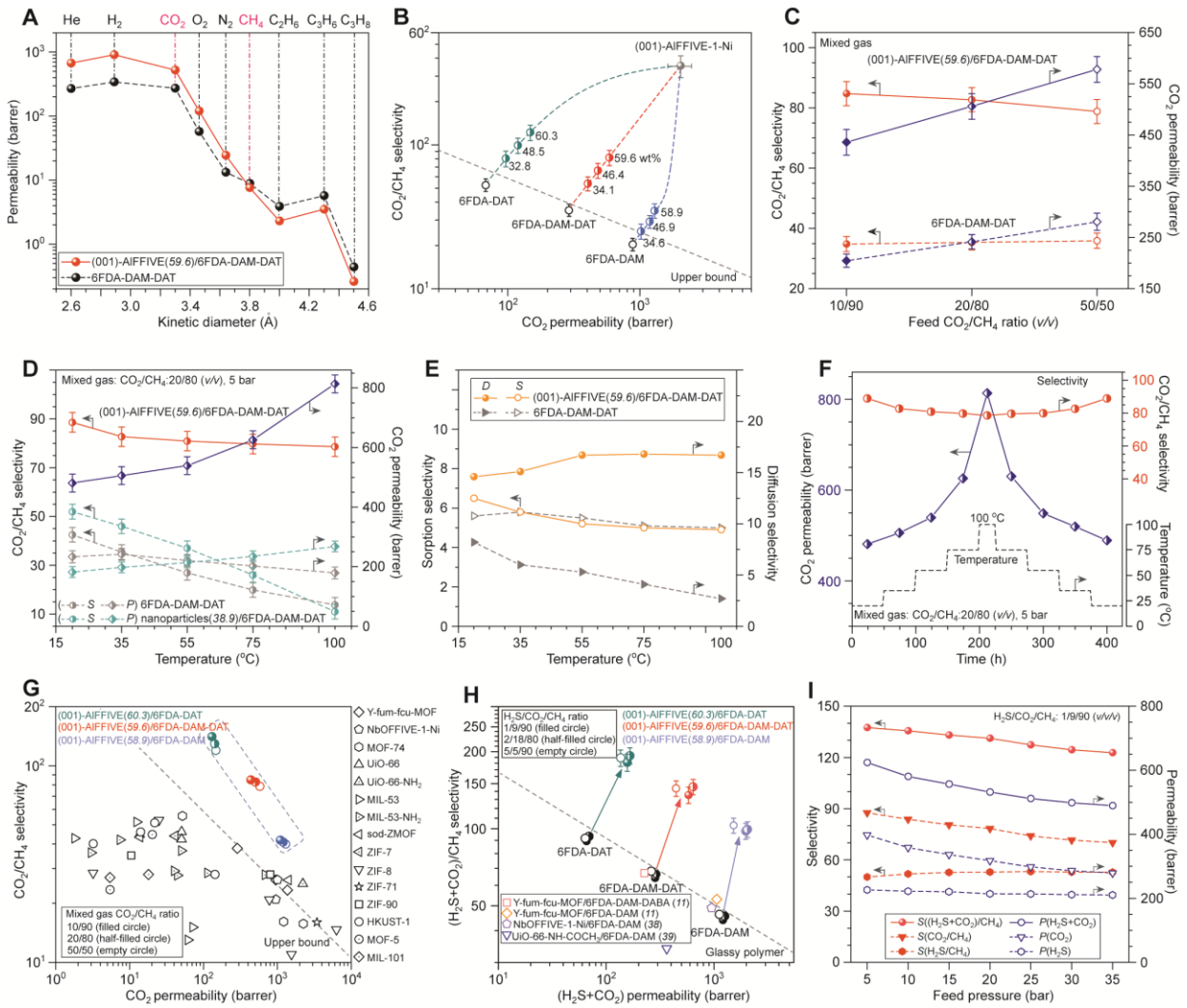

Fig. 4. Gas separation properties. (**A**) Gas permeability of gases with various kinetic diameters. (**B**) CO_2 permeability and CO_2/CH_4 selectivity of [001]-oriented MMMOF membranes with various nanosheets loading in wt% and predicted pure (001)-AlFFIVE-1-Ni membrane; pure gas permeation (CO_2 at 1 bar and CH_4 at 4 bar, 35 °C). (**C** and **D**) Effects of feed CO_2 concentration and temperature on CO_2 permeability and CO_2/CH_4 selectivity for [001]-oriented and pure polymeric membranes, mixed-gas permeation (CO_2/CH_4: 50/50 at 2 bar, 20/80 at 5 bar, and 10/90 at 10 bar, 35 °C) (C) and temperature region between 20 and 100 °C (D). (**E**) Variation of CO_2/CH_4 sorption and diffusion selectivity with respect to temperature between 20 and 100 °C. (**F**) Long-term stability and reversibility of CO_2 permeability and CO_2/CH_4 selectivity under thermal stress in (001)-AlFFIVE(*59.6*)/6FDA-DAM-DAT membrane. (**G**) Plot of CO_2/CH_4 selectivity versus CO_2 permeability providing a recent literature review of polymer/MOF-based MMMs. (**H**) $(H_2S+CO_2)/CH_4$ mixed-gas separation properties of [001]-oriented and pure polymer membranes, and comparison with the literature; permeation conditions and individual H_2S and CO_2 permeability and H_2S/CH_4 and CO_2/CH_4 selectivity are listed in Supplementary Table 16. The dash black line indicates the general trade-off between permeability and selectivity in glassy polymers under the described test condition. (**I**) Permeability and selectivity of [001]-oriented membrane under feed pressures between 5 and 35 bar, at 35 °C. The dash black line in Fig B and G indicates the Robeson upper bound for state-of-the-art polymer membranes ref (*3*). The average permeation data are presented; error bars represent the standard error of three membranes (n = 3). 1 barrer = 10^{-10} cc(STP) cm cm^{-2} s^{-1} $cmHg^{-1}$.